Supplementary materials

1.ShellSet.[1]

Figures 1,2,and 3 comprehensively illustrate ShellSet's performance advantages in parallel computing, covering single-model thread optimization, multi-model parallel efficiency on desktop computers, and scalability on high-performance computing (HPC) clusters.

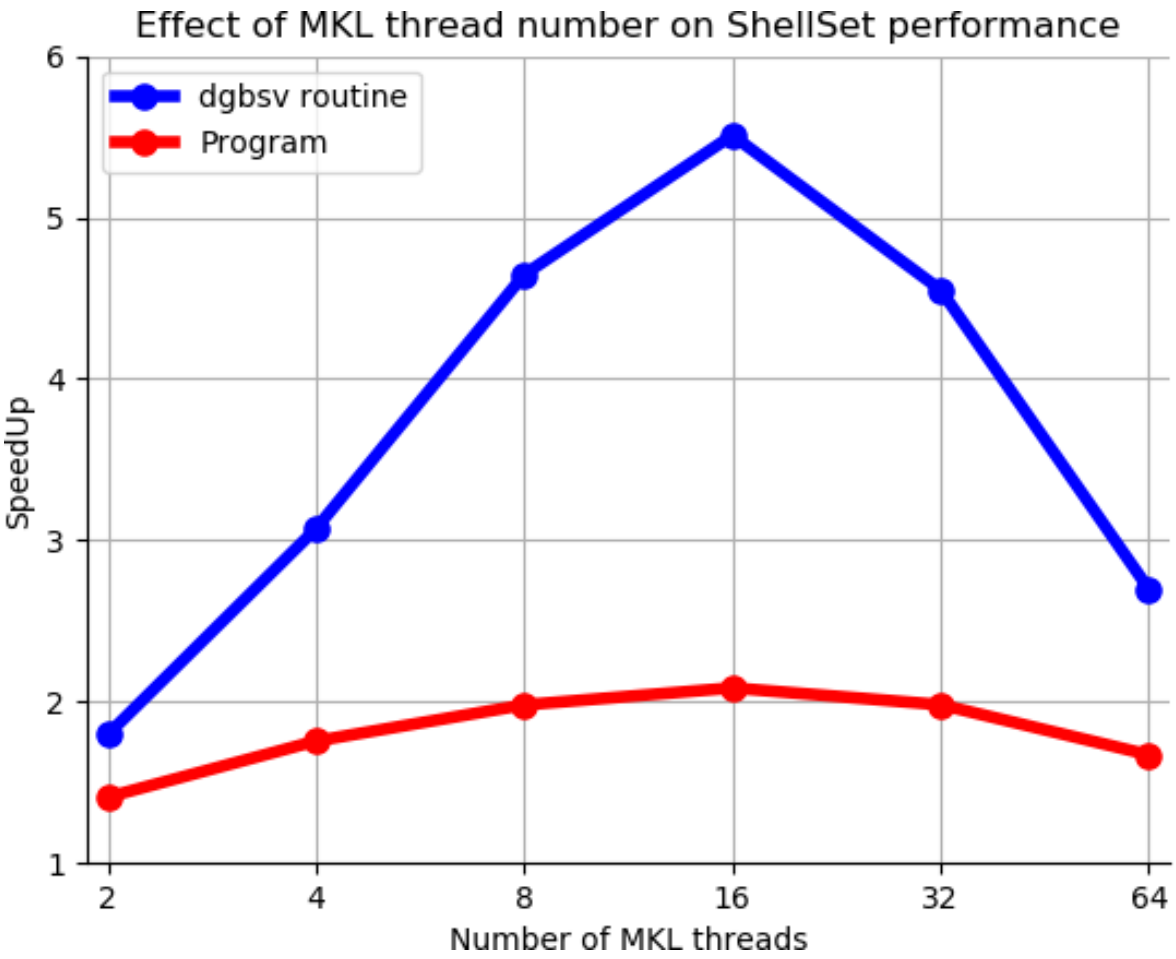


Figure S1. Speedup plot for the dgbsv routine and program using 2-64 MKL threads.

This figure plots the speedup of the core dgbsv routine and the entire program against the number of Intel MKL threads (ranging from 2 to 64) on a 64-core HPC node. The speedup grows significantly as threads increase from 1 to 16—reaching 5.51 for the dgbsv routine and 2.09 for the whole program. Beyond 16 threads, performance degrades. The optimal MKL thread count for single-model runs is 16, as excess threads cause cross-CPU memory access overhead. This provides a critical tuning guideline for maximizing single-model computational efficiency.

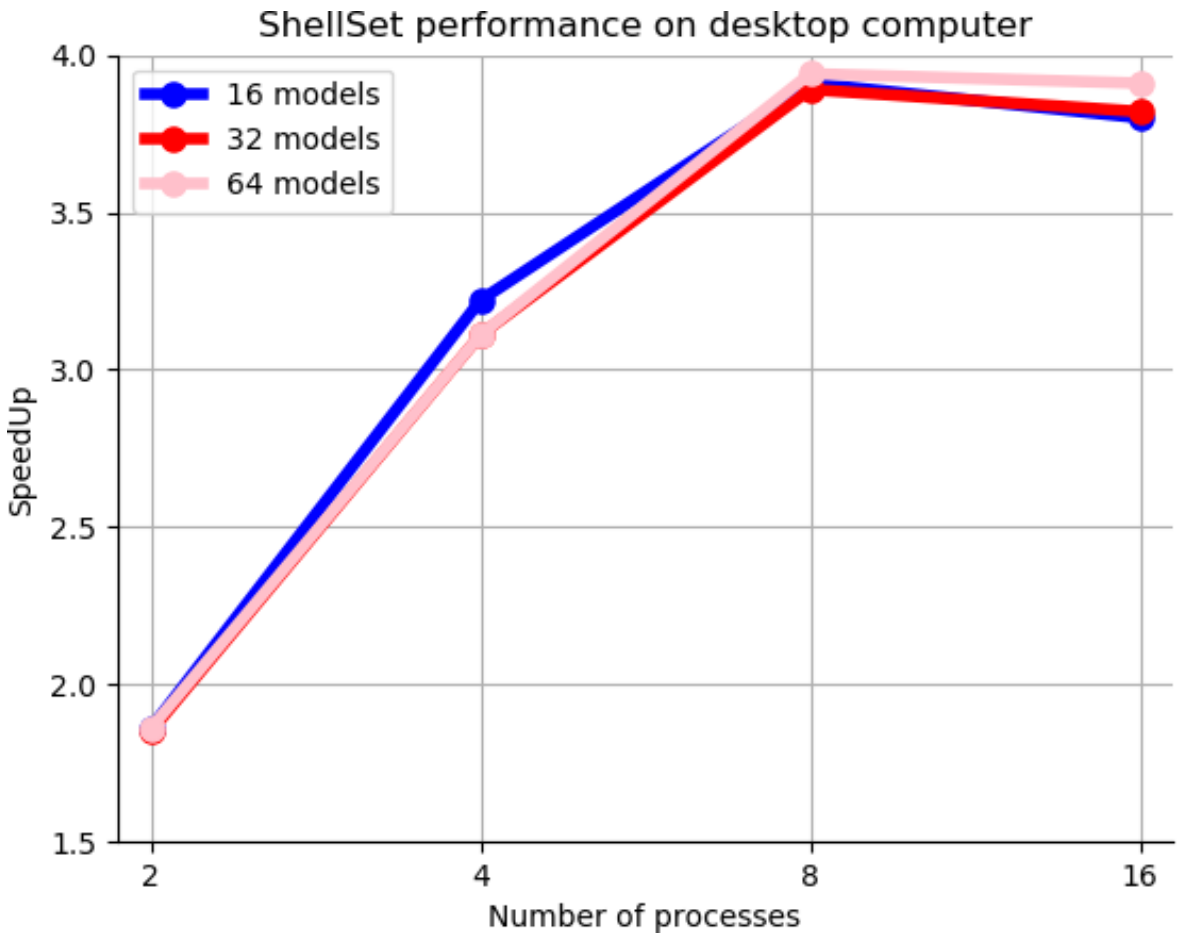


Figure S2. Speedup plot for 2, 4, 8 and 16 workers performing 16, 32 and 64 models, on a desktop machine

This figure shows the speedup of running 16, 32, and 64 models with 2–16 parallel worker processes on an Intel Core i9-12900 desktop (16 physical cores, 24 threads).Speedup peaks at 3.94 (for 64 models with 8 processes) and remains stable around 3.8–3.9 for more processes. For 4 processes, the speedup reaches ~3.3, close to the ideal linear speedup. Performance plateaus beyond 8 processes due to memory bandwidth constraints. ShellSet delivers substantial efficiency gains on standard desktops. Even with limited hardware, running 4–8 parallel processes can reduce multi-model simulation time by up to 75%, making it accessible for routine research.

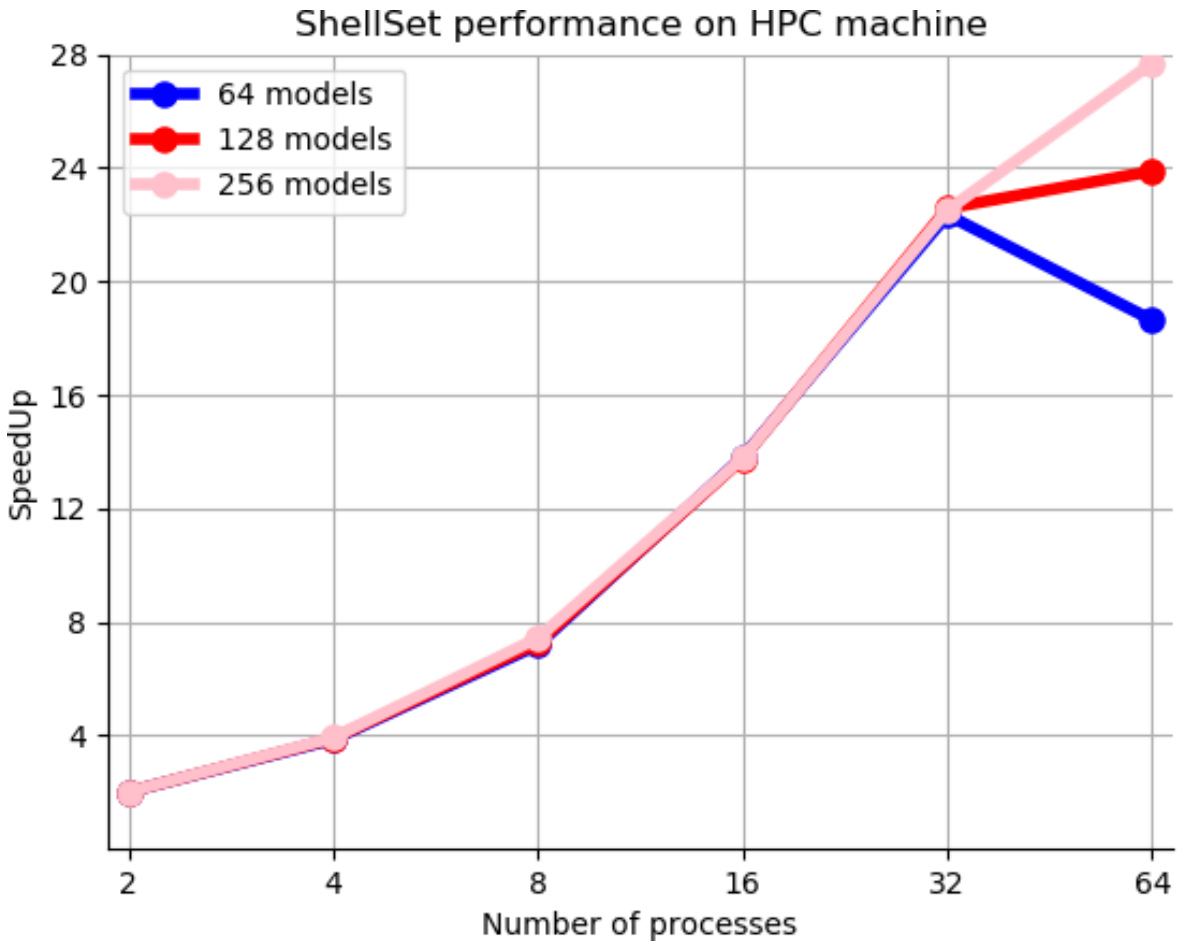


Figure S3. Speedup plot for 2, 4, 8, 16, 32 and 64 workers performing 64, 128 and 256 models, on a 64-core node of a HPC machine.

This figure presents the speedup of running 64, 128, and 256 models with 2–64 worker processes on a 64-core HPC node (four Xeon Gold 5218 CPUs).The speedup scales nearly linearly with process count up to 32 processes. For 64 processes, the speedup reaches 27.69 for 256 models—almost 30x faster than serial execution. Only when the node is fully loaded (64 processes) does performance vary slightly across model counts. ShellSet exhibits excellent scalability on HPC clusters, enabling efficient large-scale parameter searches. It fully leverages distributed memory architectures, making it suitable for complex global neotectonic simulations.

1. May, J.B.; Bird, P.; Carafa, M.M.C. ShellSet v1.1.0 parallel dynamic neotectonic modelling: a case study using Earth5-049. *Geosci. Model Dev.* **2024**, *17*, 6153-6171.

2. Ellipsis3D[2]

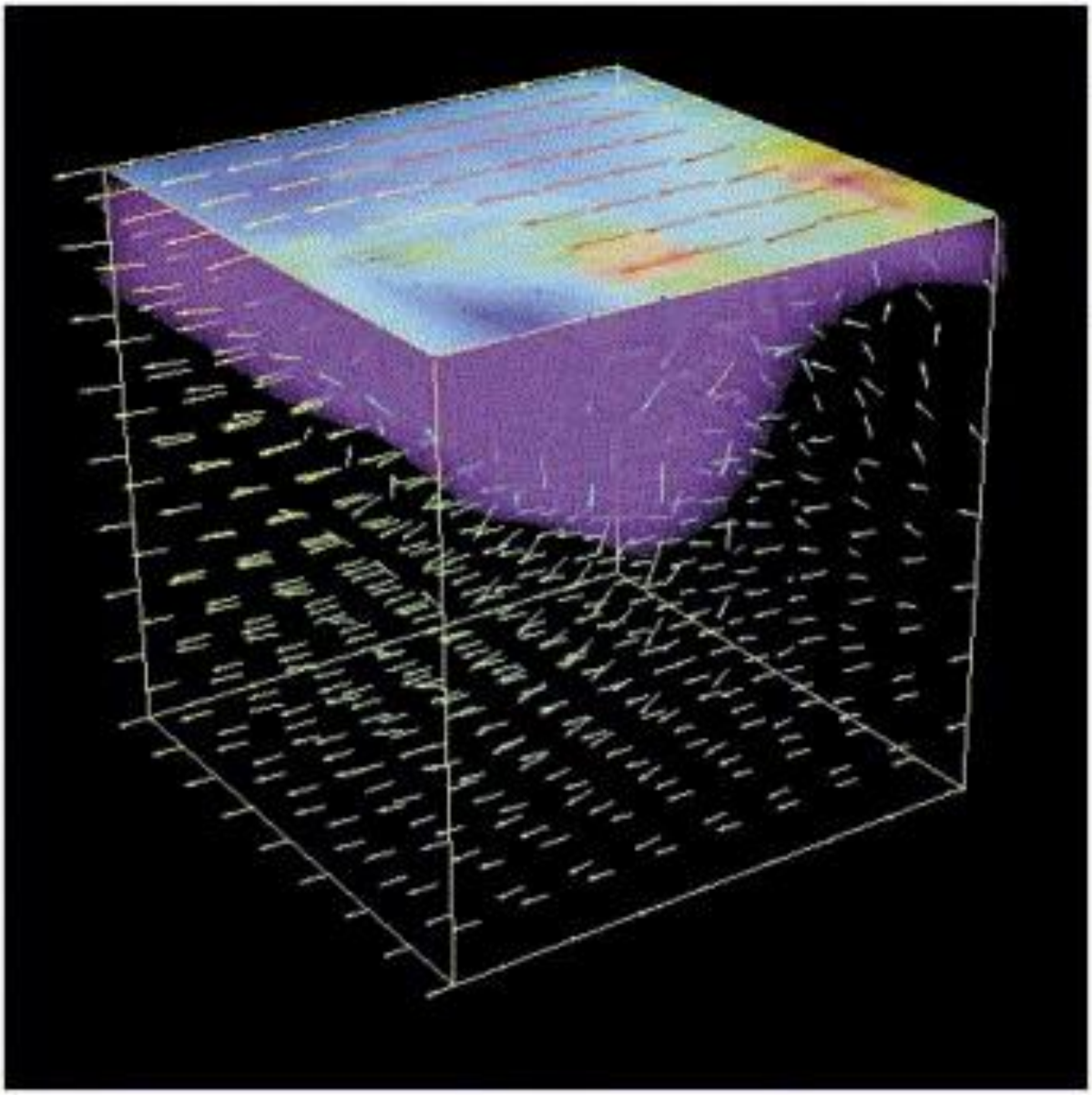


Figure S4. Oblique forced subduction: Lithosphere is shown as purple, and the nodal velocities are shown as arrows. The surface colourfield indicates regions of high accumulated distortional strain.

This figure effectively simulates the large deformation process of lithospheric subduction, accurately captures the regions with high strain accumulation in subduction zones, and verifies the software's numerical implementation capability for viscoplastic rheology and strain weakening mechanisms; The collaborative application of periodic boundary conditions and reflective boundary conditions demonstrates the software's flexibility in complex boundary settings, making it suitable for large-scale geological processes such as plate motion.

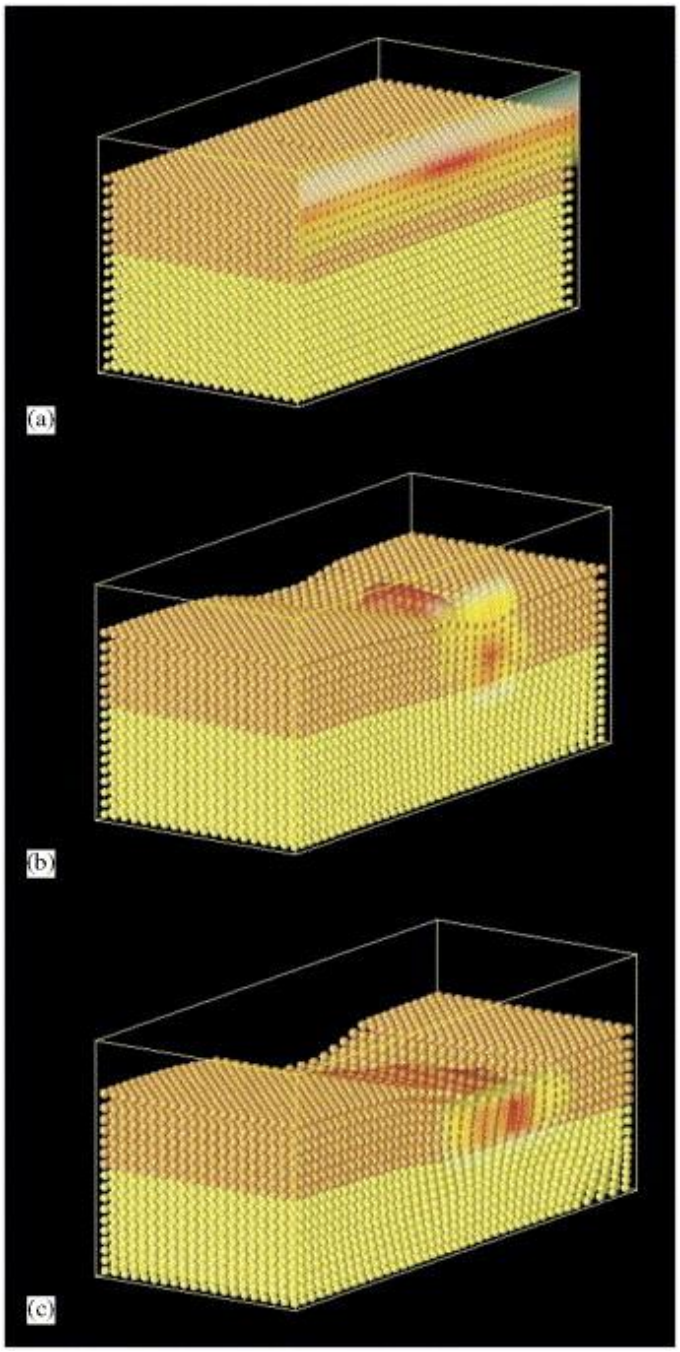


Figure S5. three-layered crustal extension model, with a brittle upper crust, ductile lower crust, and compressible air layer. Orange spheres denote the upper crust, and yellow spheres denote the lower crust. Plastic strain is also shown, either as a superposed translucent grid on the right side of the box, and as a red translucent contour surface delineating the areas with a plastic strain of 0.2

This figure achieves the mechanical coupling simulation of multiple materials (brittle, ductile, and compressible fluid), accurately reproducing the differential behaviors of brittle fracture in the upper crust and ductile flow in the lower crust during crustal extension; The dynamic mesh extension technology adapts to the "stretching-filling" process of crustal extension, and the particle splitting/fusion mechanism ensures the resolution of deformed regions, demonstrating the software's adaptability to unsteady and large-scale tectonic movements.

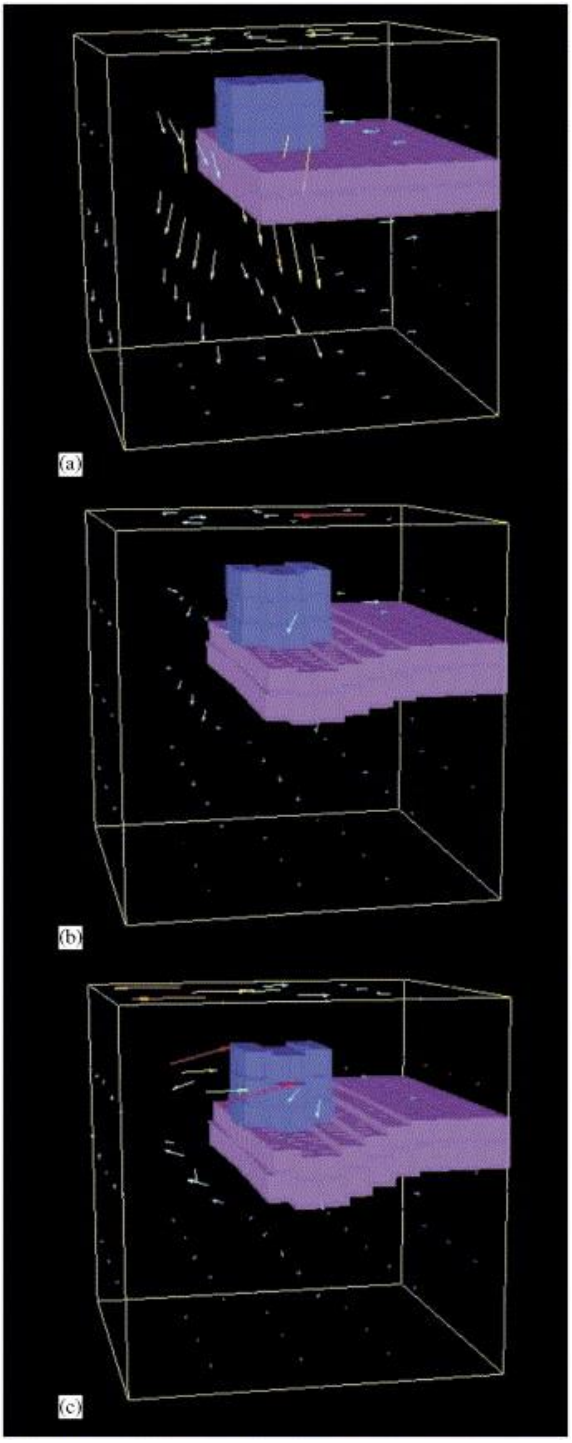


Figure S6. lexure of a viscoelastic plate (plate is purple): The plate has a density of 3300 kg/m3 . The load (blue) has similar physical properties, but with a density of 8000 kg/m3 Arrows denote the velocity

This figure accurately simulates the time-dependent deformation of viscoelastic materials (instantaneous elastic response + viscous creep), which is highly consistent with geological scenarios such as mantle plume loading and seamount loading, verifying the software's numerical stability for viscoelastic rheology.

2. O'Neill, C.; Moresi, L.; Müller, D.; Albert, R.; Dufour, F. Ellipsis 3D: a particle-in-cell finite-element hybrid code for modelling mantle convection and lithospheric deformation. Computers & Geosciences 2006, 32, 1769-1779.

3. SLIM3D[3]

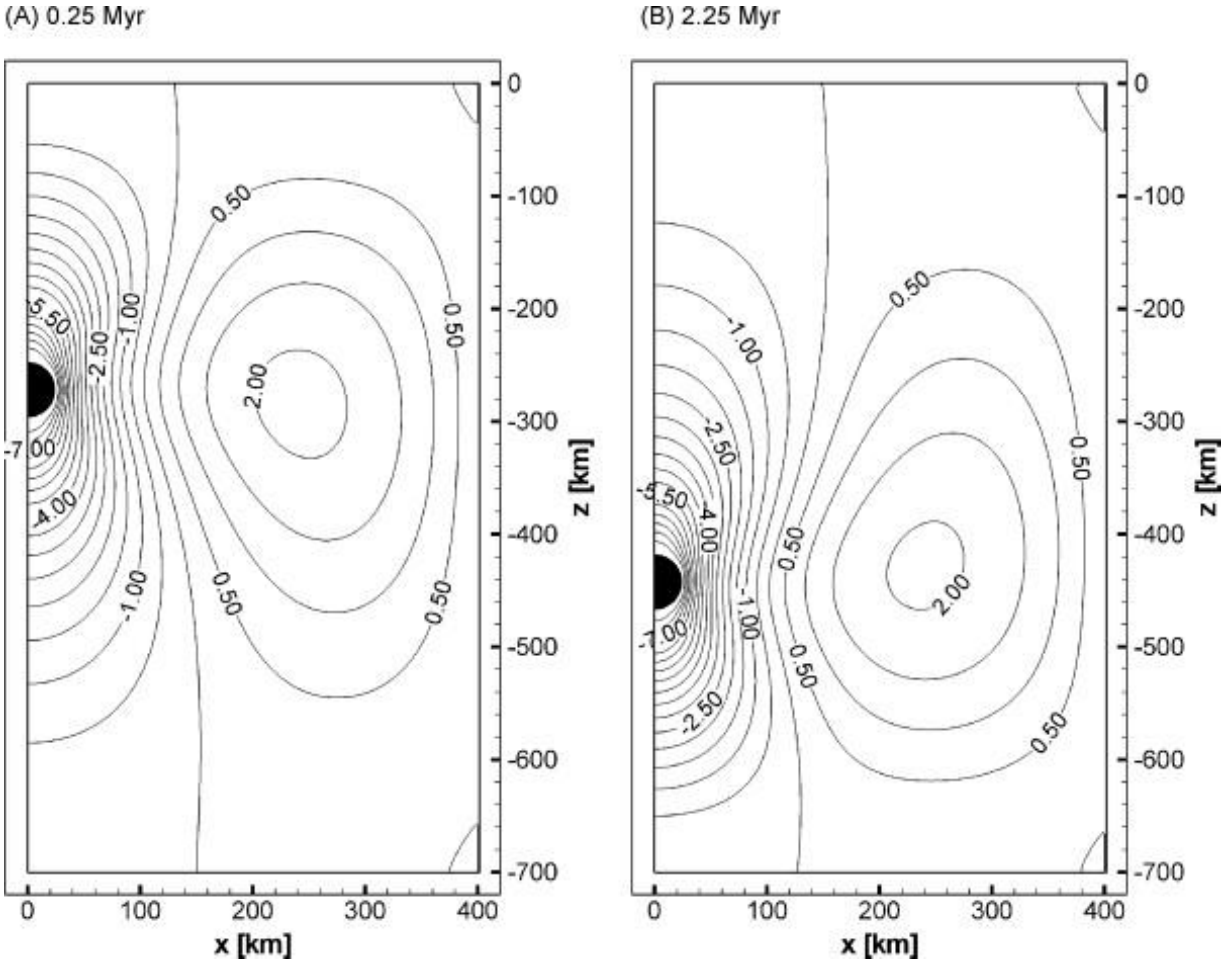


Figure S7. Isolines of vertical velocity for the cylinder problem. (A) After 0.25 Myr, (B) after 2.25 Myr. Black circles indicate positions of the particles which represent the cylinder.

This figure accurately simulates viscous flow under large viscosity differences (cylinder viscosity: 10^{24} Pa·s vs. fluid viscosity: 10^{20} Pa·s), with a relative error of only 1.7% between the calculated sinking velocity of the cylinder (8.61 cm/year) and the analytical solution (8.47 cm/year), verifying the high precision of viscous rheology simulation. The re-gridding and material remapping technologies efficiently track the cylinder shape, which still maintains a circular boundary without obvious numerical diffusion after hundreds of remapping cycles, making it suitable for long-term geological processes such as subducting slab sinking and mantle plume ascent.

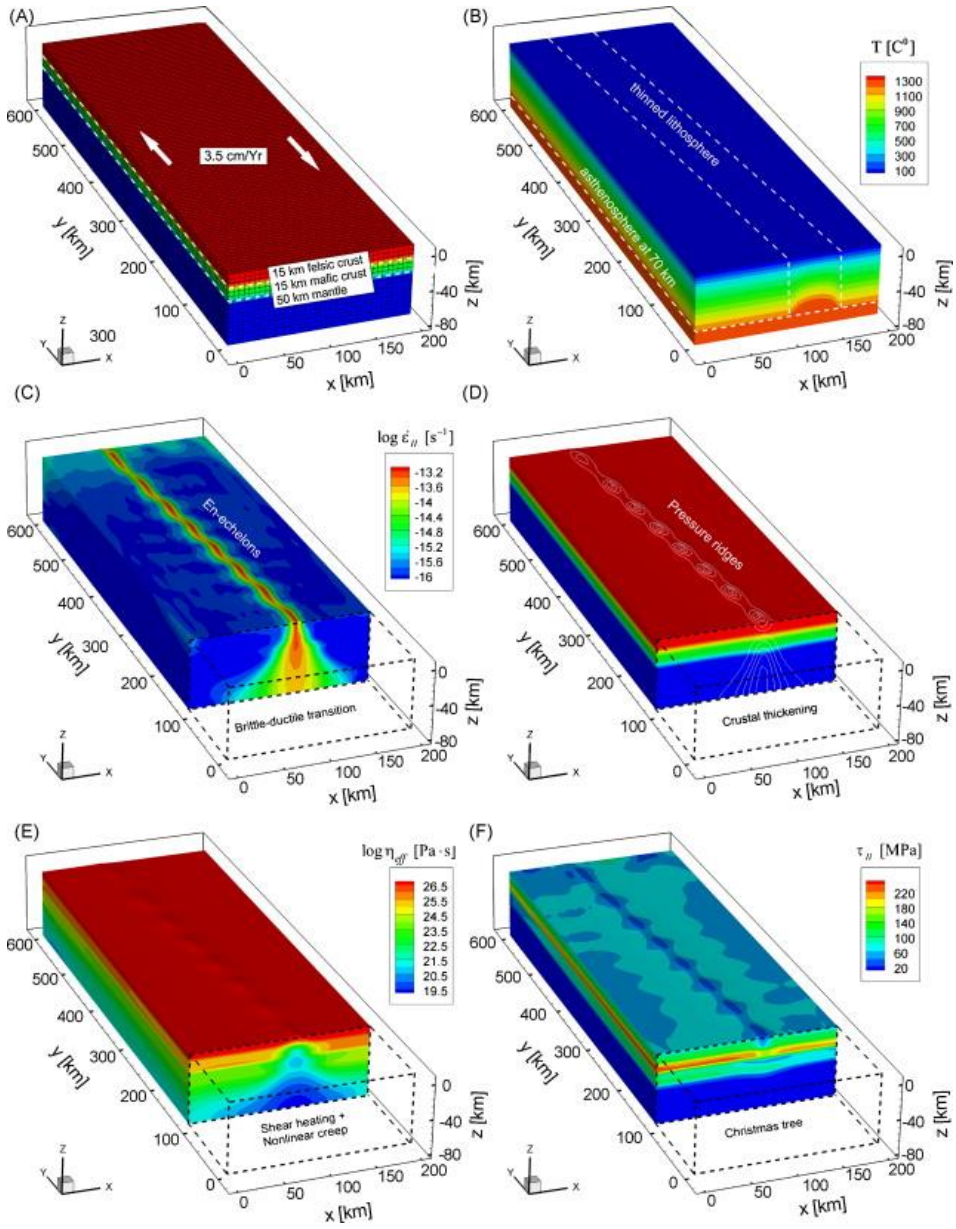


Figure S8. Lithospheric transpressional deformation problem. (A) Setup and discretization, (B) initial thermal model, (C) distribution of effective strain rate on the surface and in the cross-section after 3 Myr, (D) material phases (colors) and vertical displacements (white lines), (E) distribution of effective logarithmic viscosity (F) effective stress.

This figure achieves the comprehensive simulation of elasto-visco-plastic rheology, thermo-mechanical coupling, free surface, and Winkler foundation boundary, adapting to the long-term tectonic evolution of lithospheric scale (spatial range: 200-600 km, temporal scale: 3-6 million years). It accurately reproduces the layered differential behaviors of "brittle faults in the upper crust - ductile flow in the lower crust - viscoelastic deformation in the mantle", captures key processes such as shear heating and strain weakening, and verifies the software's capability in handling multi-scale and multi-mechanism coupling problems.

3. Popov, A.A.; Sobolev, S.V. SLIM3D: a tool for three-dimensional thermomechanical modeling of lithospheric deformation with elasto-visco-plastic rheology. Physics of the Earth and Planetary Interiors 2008, 171, 55-75.

4. I3ELVIS[4]

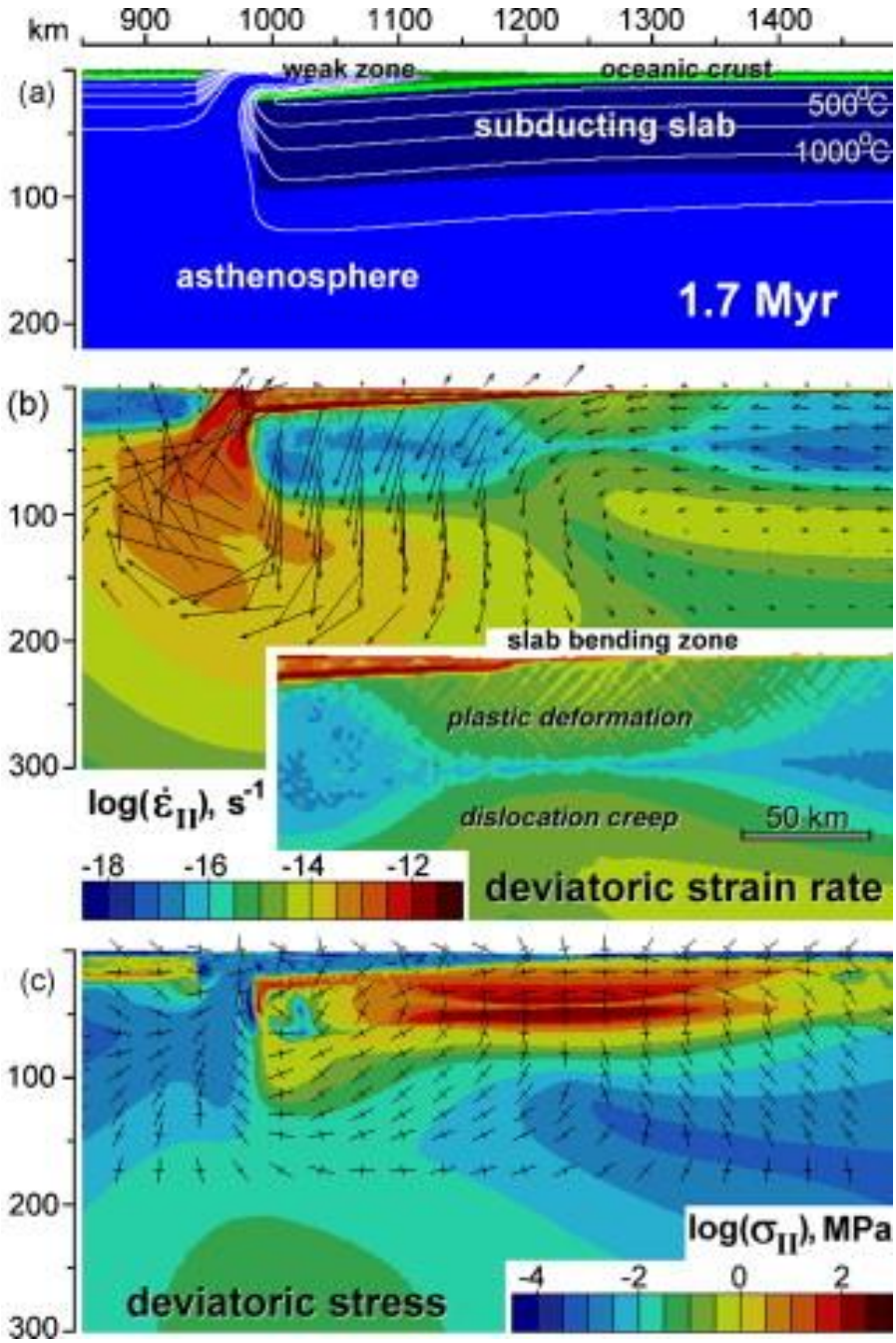


Figure S9. 640 × 300 km high-resolution (320 × 90 nodes, 120,000 markers) area of original 3000 km × 2500 km model with non-uniform numerical grid (520 × 164 nodes, 4,570,000 randomly distributed markers) is shown. Two plates of different ages (1 and 70 Myr for the left and right plate, respectively) are juxtaposed together along the transform fault. Initial zone of wet fractured rocks (c.f. light blue zone in (a)) with low plastic strength ($\sin(\varphi) = 0$) was present along the fault that created favorable conditions for spontaneous initiation of subduction (Hall et al., 2003) and slab bending. (a) Distribution of different rock types (color code) and isotherms (white lines); (b) strain rate (color code) and velocity (black arrows) distribution, zoom-in shows slab bending area; (c) deviatoric stress distribution (color code) and stress principal axis orientation (elongated crosses, long and short branches of the crosses show extension and shortening directions, respectively)

This figure supports large-deformation simulations of materials with strong rheological contrasts (high viscosity of plate rocks and low viscosity of the asthenosphere) and enables the spontaneous formation of narrow shear zones (1–2 grid cells wide).It accurately couples complex rheological mechanisms such as plastic yielding and dislocation creep, making it suitable for high-precision simulations of key geological processes including subduction zone bending and fault development. This demonstrates the software's adaptability to long-term geological evolution (on the million-year timescale).

4. Gerya, T.V.; Yuen, D.A. Robust characteristics method for modelling multiphase visco-elasto-plastic thermo-mechanical problems. Physics of the Earth and Planetary Interiors 2007, 163, 83-105.

5. SNAC[5]

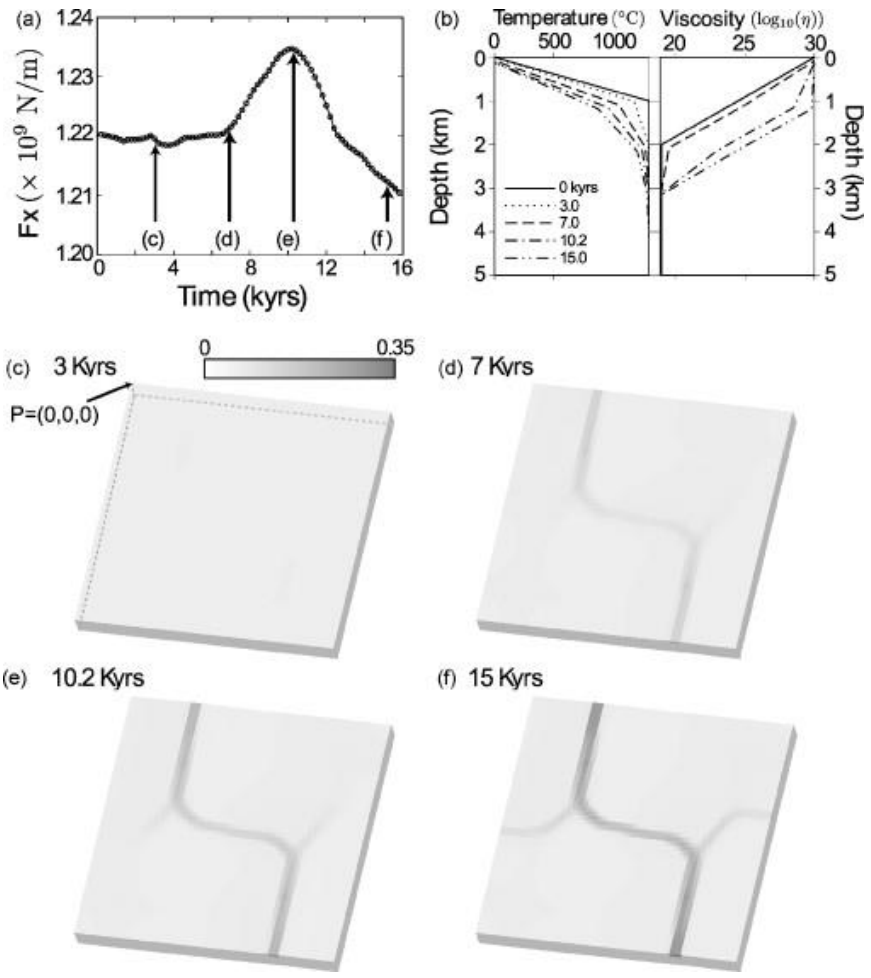


Figure S10. (a) F_x, force required to extend the domain at the applied velocity in the *x*-direction as a function of time. (b) Depth profiles of temperature and viscosity are taken at the point *P* marked in (a) and compared at different time steps (0, 3, 7, 10.2, and 15 kyears). The rise in F_x at ~7 kyears coincides with the cooling and significant increase in viscosity of the subsurface (1–2 km deep) layer. 3D rendering of the second invariant of plastic strain at the same set of time steps: (c) 3 kyears, (d) 7 kyears, (e) 10.2 kyears, and (f) 15 kyears.

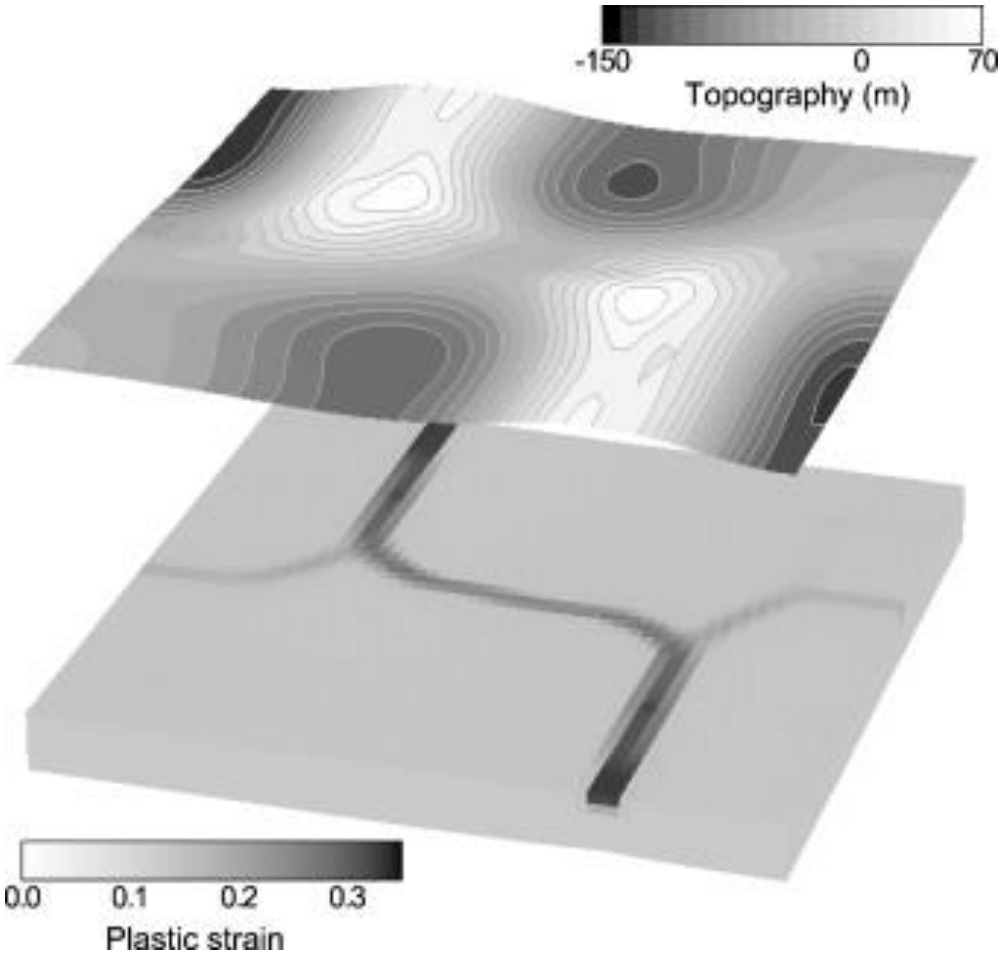


Figure S11. A 3D representation of the surface topography from the base model at 15 kyears on top of the model domain. Plastic strain on the surface of the model domain indicated through grey scale shading.

Figure 10 and Figure 11 achieves deep coupling f the thermal and mechanical fields — rock cooling leads to increased viscosity, which in turn causes an increase in system stiffness, ultimately manifested as an abrupt change in the external force F_x. This fully reproduces the "thermal-viscosity-stress" transmission chain. The consistency between the plastic strain distribution and topographic morphology demonstrates the software's uniformity in the coordinated output of multiple physical quantities, enabling it to directly provide numerical prediction bases for geophysical observations such as topography and gravity.

5. Choi, E.-s.; Lavier, L.; Gurnis, M. Thermomechanics of mid-ocean ridge segmentation. *Physics of the Earth and Planetary Interiors* **2008**, *171*, 374-386.